The Polarized Emissivity of a Wind-Roughened Sea Surface: A Monte Carlo Model

Bradley G. Henderson [a], James Theiler [a], Pierre Villeneuve [a,b]

[a]*Space and Remote Sensing Sciences Group, NIS-2, Los Alamos National Laboratory, Los Alamos New Mexico 87545*

[b]*Now at Space Computer Corporation, Los Angeles, CA*

Abstract

We use a Monte Carlo ray-tracing model to compute the thermal-infrared emissivity of a wind-roughened sea surface. The model includes the effects of both shadowing and the reflected component of surface emission. By using Stokes vectors to quantify the radiation along a given ray path, we compute the effects of polarization as well. We separate the direct emission from surface reflections to show how each affects the nature of the emitted field. The reflected component is an important part of the radiative transfer and affects nearly 10% of the ray paths at emission angles between 60° and 80° at wind speeds $\gtrsim$ 5 m/s, increasing the effective emissivity by as much as 0.03. The modeled emissivities agree nicely with recent sea surface emissivity measurements. We also compare the Monte Carlo results to a recently published analytic model and show that the two vary somewhat due to differences in the amount of the reflected component included in the calculations. Surface roughness has a large effect on the polarization between 60° and 90° but less so at smaller angles. Including the reflected component has a small but noticeable effect which actually enhances the degree of polarization at intermediate angles.

Key words: Emissivity, thermal infrared, SST, polarization

1 Introduction

A number of current and future remote sensing platforms will retrieve sea-surface temperature (SST) from inversion of multi-spectral infrared thermal emission data. The algorithms used to compute SST rely on the fact that the emissivity of water is well known in the thermal infrared and varies little with surface condition. This assumption seems to be valid for nadir viewing,

but at higher emission angles, there is increased potential for variability. The standard model (Masuda et al., 1988) for computing the directional emissivity of water predicts that the surface emissivity decreases with surface roughness out to about 60 degrees, whereas existing measurements show that roughness increases the emissivity at all angles (Schott et al., 1991). This discrepancy is likely due to the fact that the reflected component of the emitted field is not included in many rough surface emissivity models (Fig. 1). This component arises when infrared photons emitted by a portion of the wave surface strike an adjacent or nearby facet and are re-directed toward the sensor. Near nadir, wave slopes of 45° are needed for reflected photons to reach the sensor, which are negligible even for high wind speeds (Cox and Munk, 1954). However, reflections become significant at emission angles greater than 50° (Otterman et al., 1992). Sensors such as the Along Track Scanning Radiometer (ATSR) which view the sea surface at higher emission angles need accurate emissivity models for use in multi-angle SST retrieval (Barton et al., 1989; Tornow et al., 1994).

Some recent models have included the effects of reflections (termed "SESR," which stands for "surface-emitted surface-reflected") by adding an additional term to an analytic expression for the effective emissivity (Watts et al., 1996; Wu and Smith, 1997). Inclusion of the SESR term significantly improves the accuracy of the computed emissivity, especially at higher emission angles. Analytic models have the advantage that they are fairly easy to implement. One disadvantage, however, is that the simplicity requires a number of assumptions to be made about the nature of the sea surface. For example, in order to compute the contribution from SESR effects, it is necessary to know the sea slope statistics as seen by any potential reflecting facet on the surface. The two analytic models mentioned above used the standard Cox and Munk (1954) statistics which, strictly speaking, apply to large patches of the sea surface when viewed high in the sky and do not necessarily hold for a viewing point *on* the surface, such as inside a wave trough. Furthermore, a wave facet which reflects photons toward the sensor has a field of view (*i.e.*, the 2π space above it) which is part sea surface and part sky. To isolate the source of the reflected photons, one must pick an angle, measured from the zenith, which defines the boundary between sea and sky. This angle will vary with the position on the wave surface and the sea state, which creates a bit of uncertainty when computing the SESR component.

An additional physical phenomenon which becomes important at high emission angles is shadowing. Shadowing occurs when certain parts of the sea surface are not visible because they are obstructed by wave crests which lie in between the sensor and the shadowed region (see Fig. 1). The photons emitted by a shadowed facet will not reach the sensor because they are blocked by the intervening wave crest. Saunders (1967) developed a shadowing algorithm for application to reflected skylight and later used it to compute the

thermal-infrared radiance of the ocean horizon (Saunders, 1968). Solving the problem analytically is not trivial, and as a result, simplifying assumptions must be made in order to make the problem tractable. An assumption made by Saunders (1967) which crops up frequently in related work is that all wave slopes are shadowed equally. Although this seems intuitive for horizontal or gently dipping slopes, it seems less likely for steeper slopes (Saunders, 1967).

We have developed a Monte Carlo ray-tracing model to compute the emissivity of computer rendered, wind-roughened sea surfaces. The use of a ray tracing method allows us to include both the reflected emission and shadowing and furthermore permits us to examine more closely how these processes control the radiative properties of the surface. The intensity of the radiation along a given ray path is quantified using Stokes vectors, and thus polarization is explicitly included in the calculations as well. The polarized emissivity of a rough water surface in the infrared was treated previously by Sidran (1981) and Hall (1964). However, the polarization can be affected significantly by the reflected component, which, to our knowledge, has not been examined before. In the first part of the paper, we describe the surface model and the ray tracing algorithm used to compute the surface emissivity. In the following section, we present the results for the directional and spectral emissivity and compare them to recently published sea surface emissivity data and a recent analytic model. Next, we present the computed polarization and show specifically how surface roughness and reflections each affect the polarization state of the emitted radiation.

2 Model Description

2.1 Surface Model

To simulate a wind-roughened sea surface, we used the random capillary model of Preisendorfer and Mobley (1985) and Preisendorfer and Mobley (1986). We will describe the surface here briefly for completeness. The reader is encouraged to see the cited references or Mobley (1994) for a more thorough description.

Construction of the surface begins with a planar grid of points which defines the vertices of a collection of interlocking isosceles triangles, or "triads." Each point in the grid is assigned a height from a Gaussian distributed population of random numbers with zero mean and variance σ^2. The heights associated with the three points in a triad define one facet, the collection of which forms one realization of a random capillary wave surface. The upwind and crosswind dimensions of the triangles, δ and ε, respectively, and the variance σ^2 of the population, are defined as follows:

$$\delta = 1$$
$$\varepsilon = [3a_{\mathrm{u}}/4a_{\mathrm{c}}]$$
$$\sigma = [(a_{\mathrm{u}}/2)U] \tag{1}$$

in which the upwind and crosswind constants a_{u} and a_{c} are given by

$$a_{\mathrm{u}} = 3.16 \times 10^{-3} \text{ s/m}$$
$$a_{\mathrm{c}} = 1.92 \times 10^{-3} \text{ s/m} \tag{2}$$

and U is the wind speed in meters per second measured at a height of 12.5 m above sea level. With these definitions, the upwind and crosswind slopes of the realized surface(s) will obey the wave slope wind speed law of Cox and Munk (1954):

$$P(z_x, z_y) = \frac{1}{2\pi\sigma_{\mathrm{u}}\sigma_{\mathrm{c}}} \exp\left[-\frac{1}{2}\left(\frac{z_x^2}{\sigma_{\mathrm{u}}^2} + \frac{z_y^2}{\sigma_{\mathrm{c}}^2}\right)\right] \tag{3}$$

where z_x and z_y are the slopes ($\partial z/\partial x$ and $\partial z/\partial y$) in the upwind and crosswind directions, respectively, and σ_{u}^2 and σ_{c}^2 are the associated variances given by

$$\sigma_{\mathrm{u}}^2 = a_{\mathrm{u}}U$$
$$\sigma_{\mathrm{c}}^2 = a_{\mathrm{c}}U. \tag{4}$$

An example of this type of surface is shown in Fig. 2. The surface shown in this figure was constructed from a 6×6 grid. The grid size used in the actual calculations was set to be large enough that no reflected rays went beyond the lateral edges of the surface before having ample opportunity to intersect other facets. Repeated trials on very large surfaces showed that a 20×20 grid was more than adequate when the "target" facet was at the center of the surface (*i.e.*, the rays were aimed at the central facet). Fig. 3 shows a 3-d subsection of one facet, along with the associated angles and viewing geometry.

Although the above described surface obeys the wave slope statistics derived by Cox and Munk, it does not reproduce water surface height statistics as given by an actual wave spectrum (*e.g.*, Pierson and Moskowitz (1964); Jähne and Riemer (1990); Liu and Yan (1995); Elfouhaily et al. (1997)). Wave heights in a random capillary model are uncorrelated from facet to facet, and thus some effects such as shadowing at near-grazing emission angles (Saunders, 1967; Theiler and Henderson, 1997) may not be modeled correctly. In fact, the Cox-Munk equations break down on the horizon and predict infinite radiance for reflected sunlight (Zeisse, 1995). However, the wave slopes given by Cox-Munk statistics are consistent with the wave slopes derived from a full gravity-capillary wave spectrum. Thus, the radiative transfer modeled here should be

accurate for non-grazing emission angles. For further discussion, see Mobley (2002).

2.2   Ray Tracing

The basic ray-tracing algorithm employed for the model was motivated by the need to compute the emissivity at any selected viewing geometry. The method and mechanics are similar to that of Henderson et al. (1992), in which the polarized thermal emission from a particulate surface was computed; interested readers are invited to see that reference for additional information and applications. The equations and the method will be presented here completely for later reference.

A real sea surface is emitting IR radiation continuously into the half space above it. To model its emissive properties using a ray tracing model, one could use a "forward" method in which individual rays are launched from random facets in random directions, and their geometry tracked as they bounce between wave crests and finally leave the surface. However, a wind-roughened water surface is a complex multi-scale surface with essentially an infinite number of possible ray path geometries leaving the surface. Sampling all geometries with adequate statistics would thus require a tremendous number of rays.

Alternatively, we use a reverse approach to compute the emitted ray paths (Collins et al., 1972). Rather than start at some random location on the surface and track ray paths of actual photons leaving the surface, we track ray paths which propagate *toward* the surface along a pre-selected trajectory. We record its geometry as it bounces from facet to facet and stop when it reflects back to the sky. We then compute the radiation emitted by the surface along that ray path by traversing it in the opposite direction. This procedure is repeated in a Monte Carlo fashion to obtain multiple ray paths which all exit the surface at a pre-selected emission angle. The effective emissivity of the surface at that particular emission angle is then given by the averaged intensity of all these ray paths.

To begin a model run, we start at a point above the surface and move downward toward the central facet along a ray path predefined by the angle θ_e that the ray makes with the normal $\mathbf{N}$ to the average surface (the angle θ_e will eventually be the emission angle for the ray path, see Fig. 4a). When the ray strikes a facet, its local angle of incidence i is recorded, and its subsequent trajectory is defined by specular reflection. We repeat this procedure facet by facet until the ray bounces back to the sky or reaches a set maximum number of reflections (the impact of this parameter will be discussed further). We then calculate the intensity of the radiation emitted along that same ray path by

5

traversing it in the opposite direction. We go to the point of the last reflection and use that facet (the "source" facet) as the initial source of radiation along the ray (Fig. 4b). The basic idea is that if an imaginary ray can follow that path going toward the surface, then actual emitted photons can escape along the same path. The advantage of this reverse approach is that it lets us specify a desired viewing geometry at the start of a run.

At the source facet, the normal $\mathbf{n}$ and the exiting ray define the plane of emission. The angle between the normal and the ray is the local emission angle χ. Since the facet is a smooth surface, it will be a Fresnel emitter with parallel and perpendicular components ϵ_x and ϵ_y determined by the angle χ and the complex refractive index (a function of wavelength). These two values are computed from Kirchhoff's Law

$$\epsilon_x = 1 - R_x$$
$$\epsilon_y = 1 - R_y \qquad (5)$$

where R_x and R_y are the Fresnel power reflection coefficients

$$R_x = |r_x|^2$$
$$R_y = |r_y|^2. \qquad (6)$$

In the above equations, r_x and r_y are the amplitude reflection coefficients given by

$$r_x = \frac{N^2 \cos\chi - \sqrt{N^2 - \sin^2\chi}}{N^2 \cos\chi + \sqrt{N^2 - \sin^2\chi}}$$
$$r_y = \frac{\cos\chi - \sqrt{N^2 - \sin^2\chi}}{\cos\chi + \sqrt{N^2 - \sin^2\chi}} \qquad (7)$$

where N is the complex refractive index for the facet (Jackson, 1975). For this study, unless stated otherwise, we used optical constants of water from Irvine and Pollack (1968). The Fresnel emissivity of water at $\lambda = 4$ μm is shown in Fig. 5.

Next, we need to define the components of the electric vector for the emitted radiation. The Fresnel emissivities ϵ_x and ϵ_y are proportional to the electric vector intensities in the directions parallel and perpendicular to the plane of emission, respectively. The electric vector amplitudes A_x and A_y are thus proportional to the square roots of the Fresnel emissivities. We define

$$A_x = \sqrt{\frac{\epsilon_x}{2}}$$
$$A_y = \sqrt{\frac{\epsilon_y}{2}}. \tag{8}$$

Since the intensity I_e of the emitted radiation is given by the sum of the squares of the amplitudes A_x and A_y, the definition in Eqs. (8) results in the intensity being normalized to 1 when both components of emissivity are unity. These amplitudes are then used in the Stokes vector $\mathbf{S}_e$ for the emitted radiation,

$$\mathbf{S}_e = \begin{bmatrix} I_e \\ Q_e \\ U_e \\ V_e \end{bmatrix} \tag{9}$$

where the individual components are defined by

$$
\begin{aligned}
I_e &= A_x^2 + A_y^2 \\
Q_e &= A_x^2 - A_y^2 \\
U_e &= 2A_x A_y \cos \Delta \\
V_e &= 2A_x A_y \sin \Delta
\end{aligned} \tag{10}
$$

and Δ is the relative phase difference between A_x and A_y. The Stokes vector gives the complete characterization of the intensity and polarization state of the emitted radiation (Shurcliff, 1962; Kliger et al., 1990).

Transmission of blackbody energy through the surface results in partial linear polarization with the degree of polarization P_e given by

$$P_e = \left| \frac{\epsilon_x - \epsilon_y}{\epsilon_x + \epsilon_y} \right|. \tag{11}$$

Using this value, we separate the Stokes vector into polarized and unpolarized parts,

$$\mathbf{S}_e = P_e \begin{bmatrix} A_x^2 + A_y^2 \\ A_x^2 - A_y^2 \\ 2A_x A_y \cos \Delta \\ 2A_x A_y \sin \Delta \end{bmatrix} + (1 - P_e) \begin{bmatrix} A_x^2 + A_y^2 \\ 0 \\ 0 \\ 0 \end{bmatrix} \tag{12}$$

in which we take $\Delta = 0$ for linearly polarized light. $\mathbf{S}_{\mathrm{e}}$ represents the intensity and polarization state of the radiation emitted from the source facet along the first segment of the computed ray path. We can now move on to the first reflection event.

The Stokes vector $\mathbf{S}_{\mathrm{e}}$ is defined in a Cartesian coordinate system in which the x and y axes are parallel to and perpendicular to the plane of emission, respectively, and the z axis is in the direction of the ray. These coordinate axes will not necessarily be aligned with their equivalent axes at the next facet. Before reflecting $\mathbf{S}_{\mathrm{e}}$ from the facet, we must rotate it so that its x and y axes correspond to the x and y axes for the directions parallel and perpendicular to the incident plane (see Kliger et al. (1990) for the rotation matrix). Rotating the Stokes vector does not change the intensity and polarization state of the beam, but it does alter the constituent parameters A_x, A_y, and Δ. Before applying Fresnel reflection, we use Eqs. (10) to calculate the new values of A_x, A_y, and Δ in the rotated coordinate system. With this completed, we apply the Fresnel reflection coefficients to $\mathbf{S}_{\mathrm{e}}$ for the given angle of incidence and index of refraction.

The amplitude reflection coefficients r_x and r_y for a lossy medium are complex quantities:

$$
\begin{aligned}
r_x &= \rho_x \exp(i\phi_x) \\
r_y &= \rho_x \exp(i\phi_y)
\end{aligned}
\tag{13}
$$

where ρ_x and ρ_y are the magnitudes of the reflection coefficients and ϕ_x and ϕ_y are the phase changes incurred upon reflection for the parallel and perpendicular components, respectively. The amplitudes of the reflected electric vector are given by

$$
\begin{aligned}
A_{xr} &= \rho_x A_x \\
A_{yr} &= \rho_y A_y.
\end{aligned}
\tag{14}
$$

In general, the linearly polarized part of $\mathbf{S}_{\mathrm{e}}$ becomes elliptically polarized on reflection from the lossy surface, and phase difference Δ becomes $\Delta + \delta$ where $\delta = \phi_y - \phi_x$. The new values A_{xr}, A_{yr}, and Δ are then used to compute the Stokes vector for this portion of the reflected polarized (rp) radiation:

$$
\mathbf{S}_{\mathrm{rp}} = P_{\mathrm{e}}
\begin{bmatrix}
A_{xr}^2 + A_{yr}^2 \\
A_{xr}^2 - A_{yr}^2 \\
2 A_{xr} A_{yr} \cos \Delta \\
2 A_{xr} A_{yr} \sin \Delta
\end{bmatrix}.
\tag{15}
$$

The unpolarized part of $\mathbf{S}_e$ is partially linearly polarized on reflection with degree of polarization

$$P_r = \left| \frac{R_x - R_y}{R_x + R_y} \right| \tag{16}$$

where R_x and R_y are the power reflection coefficients given by Eq. (6). Using P_r, we separate the reflected linearly polarized (rlp) light from the reflected unpolarized (ru) light:

$$\mathbf{S}_{rlp} = (1 - P_e)P_r \begin{bmatrix} A_{xr}^2 + A_{yr}^2 \\ A_{xr}^2 - A_{yr}^2 \\ 2A_{xr}A_{yr} \\ 0 \end{bmatrix} \tag{17}$$

$$\mathbf{S}_{ru} = (1 - P_e)(1 - P_r) \begin{bmatrix} A_{xr}^2 + A_{yr}^2 \\ 0 \\ 0 \\ 0 \end{bmatrix}. \tag{18}$$

The three pieces are then combined into one Stokes vector $\mathbf{S}_r$ representing all the reflected radiation:

$$\mathbf{S}_r = \mathbf{S}_{rp} + \mathbf{S}_{rlp} + \mathbf{S}_{ru}. \tag{19}$$

The reflected Stokes vector $\mathbf{S}_r$ is joined by emitted radiation along the same ray path. The emitted Stokes vector $\mathbf{S}_e$ is calculated as before, and the emitted and reflected pieces are combined into one Stokes vector $\mathbf{S}$:

$$\mathbf{S} = \mathbf{S}_e + \mathbf{S}_r = \begin{bmatrix} I \\ Q \\ U \\ V \end{bmatrix} \tag{20}$$

which is separated into polarized and unpolarized parts using the degree of polarization P defined by

$$P = \frac{\sqrt{Q^2 + U^2 + V^2}}{I}. \tag{21}$$

At this point, **S** is carried to the next reflecting facet where the entire proce-
dure is repeated. The process is repeated facet by facet until the ray leaves
the surface by bouncing back to the sky. **S** is then oriented relative to a global
coordinate system at the surface in which the x axis lies in the plane defined
by the ray path and the normal **N** to the average surface. This final Stokes
vector gives the normalized intensity and the polarization state of the radia-
tion emitted and reflected along the one ray path. The normalized intensity
is equivalent to an effective emissivity of the surface for that ray path.

Using a Monte Carlo technique, we obtained a large number of ray paths, each
of which was computed on a new surface realization to assure independence
and to simulate the dynamic state of a real water surface. Stokes vectors were
computed for all of these ray paths, each of which exited the surface at the
same emission angle. The Stokes vectors were summed and averaged to yield
one Stokes vector representative of the bulk emission from the surface at that
particular emission angle. By repeating this process while varying the emission
angle and index of refraction, we computed the directional and spectral surface
emissivity and the polarization state of the emission for emission angles 0°–85°
and wavelengths 8–12 μm.

2.3   Multiple Reflections

Including the reflected component in the computation of the emitted field
tends to increase the effective emissivity for the same reason that a cavity emits
like a blackbody. With each additional reflection, the intensity of the radiation
increases, eventually converging asymptotically on the blackbody value. For
water, the emissivity in the thermal infrared is already fairly high so that not
many reflections are needed in order for the effective emissivity to converge.
Furthermore, repeated trials on our simulated water surfaces showed that the
greatest number of reflections was no more than 5 or so, which occurred at the
highest emission angles for high wind speeds. We defined a parameter called
MAXREF which set an upper limit on the number of facets a ray was allowed
to hit as it was bouncing around the surface in the reverse direction. To be
safe, when including reflections, we set $MAXREF = 10$. For comparison at the
other extreme, we sometimes set $MAXREF = 1$ which means that a reverse-
going ray was allowed to hit only one facet so that the computed emissivity
would include only the direct component and would not take into account the
effect of surface reflections.

3 Results

3.1 Directional Emissivity

Fig. 6 shows the directional emissivity of water at $\lambda = 4~\mu$m as a function of emission angle, 0°–85°, plotted for wind speeds 0, 5, 10, and 15 m/s. For clarity, the plots have been split so that the left y axis applies to angles less than 60 deg, and the right y axis applies to angles greater than 60 deg. Fig. 6a was computed with $MAXREF = 1$, which means that these curves represent only the direct component of the emission in Fig. 1 and do not take into account the effect of reflections. Fig. 6a should therefore be equivalent to the model of Masuda et al. (1988), in which the effective emissivity $\bar{\epsilon}$ is given by

$$\bar{\epsilon}(\theta_{\mathrm{e}}, \phi_{\mathrm{e}}) = \frac{1}{\cos\theta_{\mathrm{e}}} \int\limits_{-\infty}^{\infty} \int\limits_{-\infty}^{\infty} \epsilon(n, \chi)\,\cos\chi\,\sec\theta_{\mathrm{n}}\,P(z_x, z_y)\,dz_x\,dz_y,$$
$$\cos\chi > 0 \tag{22}$$

where ϵ is the average of the Fresnel emissivities given in Eq. (5) evaluated at the angle χ. The variation in emissivity with wind speed in Fig. 6a and Eq. (22) is thus due to changes in the observed slope distribution, weighted by the Fresnel emissivity, integrated over all the facets which are visible at the given viewing geometry. (Technically, the effects of shadowing are included in Fig. 6 as well but are presumably minor relative to the described viewing angle- and wind speed-dependent roughness variations.) Note that for angles $\lesssim 60°$, increased surface roughness due to increased wind speed reduces the effective emissivity. For a tessellated surface like those modeled here, each individual facet is assumed to be flat and therefore is a Fresnel emitter. The Fresnel curve (the dashed line in Fig. 5) decreases monotonically with increasing emission angle and is a maximum at 0°. Thus, for angles less than about 60°, integrating the wave-slope probability distribution, weighted by the Fresnel curve, brings in enough high-angle, low-emissivity components to reduce the effective emissivity below what it would be for a smooth surface. At higher angles, the situation is reversed with a cross-over point occurring between 65° and 70° so that above this angle, increasing surface roughness tends to increase the effective emissivity.

The above result suggests computing an effective emission angle $\bar{\chi} = \arccos\langle\cos\chi\rangle$ where

$$\langle\cos\chi\rangle = \frac{\int_{-\infty}^{\infty}\int_{-\infty}^{\infty}\cos\chi\,\sec\theta_{\mathrm{n}}\,P(z_x, z_y)\,dz_x\,dz_y}{\int_{-\infty}^{\infty}\int_{-\infty}^{\infty}\sec\theta_{\mathrm{n}}\,P(z_x, z_y)\,dz_x\,dz_y},$$

11

$$\cos \chi > 0. \tag{23}$$

In effect, $\bar{\chi}$ represents an average facet inclination, relative to $\mathbf{e}$, for a given viewing geometry and wind speed. Fig. 7 shows $\bar{\chi}$ as a function of θ_e ($\phi_e = 0$) for the four different wind speeds. When $U = 0$, $\bar{\chi} = \theta_e$, as expected for a smooth surface. As the wind speed increases and the surface gets rougher, $\bar{\chi} > \theta_e$ for $\theta_e \lesssim 68°$, and $\bar{\chi} < \theta_e$ for $\theta_e \gtrsim 68°$. This result provides additional support for our interpretation of Fig. 6. For the direct component of the emission, the effective emissivity varies with wind speed because the surface roughness changes the average facet inclination. For lower emission angles, increasing wind speed increases $\bar{\chi}$ which in turn decreases $\bar{\epsilon}$ since the Fresnel curve falls off monotonically with χ. For higher emission angles, increasing wind speed decreases $\bar{\chi}$ which in turn increases $\bar{\epsilon}$. The cross-over point between the two occurs around $68°$, just as it did in Fig. 6.

The preceding paragraphs applied to model results which did not include the effects of surface reflections. The model results in Fig. 6b were performed using a value of $MAXREF = 10$, and thus the effects of roughness, shadowing, and reflections are all included. The difference between the two is shown in Fig. 6c. Note that at low ($\theta_e \lesssim 40°$) and high ($\theta_e \gtrsim 70°$) emission angles, the plots are qualitatively the same as before—increased surface roughness decreases the effective emissivity at low angles and increases it at high angles. However, the behavior in between is quite different in that the wind speed increases the effective emissivity at intermediate angles. This effect is due to the contribution of the reflected component of the emitted field. As the fraction of reflected rays increases, the effective emissivity increases. Because the contribution of reflections increases with surface roughness, the effect is more pronounced in the 10 and 15 m/s curves, which actually cross over those for 0 and 5 m/s, keeping the spread much tighter in the region between 50 and 60 degrees.

Fig. 8 shows the fraction of reflected ray paths as a function of emission angle at the same four wind speeds. Note that at a wind speed of 15 m/s at $60°$ emission angle, nearly 10% of the ray paths have undergone reflections, which means that after being emitted from the original source facet, the ray path bounced off of at least one other facet before making it to the detector. The reflected component is thus a significant contributor to the total signal and is responsible for the increased effective emissivity seen in Fig. 6b.

3.2 Spectral Emissivity

3.2.1 Comparison with Data

Fig. 9 shows the spectral emissivity of water from 800–1200 cm^{-1}. The lines are actual sea surface emissivity spectra from Smith et al. (1996), computed from FTIR data measured from a ship at emission angles of 36.5°, 66.5°, and 73.5°. The solid lines are the mean of multiple spectra taken over the course of a day, and the dashed lines are the standard deviation ($\pm 1\sigma$). The symbols are model results computed at the same emission angles for four different wind speeds: 0, 5, 10, and 15 m/s. The modeled emissivities in Fig. 9a were computed using a *MAXREF* value of 1 (no reflections), whereas those in Fig. 9b assumed a *MAXREF* value of 10 and therefore do include reflections. Note the difference between the modeled spectra (symbols) in Fig. 9a and Fig. 9b, especially at the highest emission angle. In Fig. 9a (no reflections), the emissivity varies with wind speed by 0.04–0.05 at 73.5°. In Fig. 9b, the variation is much greater, showing a range of 0.07–0.08 between the lowest and highest wind speeds. At this emission angle, reflections are an important contributor to the total signal (see Fig. 8) and boost the effective emissivity of the surface significantly above what it would be for the direct component alone. At the other two angles, the behavior is a bit different. The spread (*i.e.*, emissivity variation with wind speed) is a bit tighter when reflections are included. On the day that the emissivity spectra were measured, the wind speed varied between 3 and 9 m/s (Smith et al., 1996) which is consistent with our modeled spectra when the reflected component is included (Fig. 9b).

3.2.2 Comparison with Analytic Model

As mentioned in the introduction, some recent analytic models have included SESR effects (Watts et al., 1996; Wu and Smith, 1997). Since analytic models are often easier to implement and less CPU intensive, it is of interest to compare those results to our Monte Carlo model.

Fig. 10a shows the spectral emissivity of ocean water from 800–1200 cm^{-1} at an emission angle of 73.5°. The dashed lines are results from the analytic model of Wu and Smith (1997), and the solid lines are the results of our Monte Carlo model. A spectrum from each model is plotted for wind speeds of 0, 1, 2, 4, 8, and 16 m/s. For aid in comparing the two, we used like symbols at a given wind speed value. To be consistent with Wu and Smith (1997), we used optical constants from Hale and Querry (1973) with the salinity adjustment from Friedman (1969) (see Masuda et al. (1988) for a listing of these values). Fig. 10b shows the spectrally averaged emissivity of both models plotted as a function of wind speed. Overall, the Monte Carlo model shows more vari-

ation with wind speed than does the analytic model. The two agree at zero wind speed, as required, but overall our computed emissivities are higher at the greater wind speeds and lower at the smaller wind speeds. Both models used the same optical constants and the same wave-slope probability distribution, which suggests that the difference is probably due to variations in the reflected component. Since including reflections tends to enhance the effective emissivity, the Monte Carlo model appears to have a higher contribution of the reflected component at high wind speeds and less at the low wind speeds, for this particular emission angle.

3.3 Polarization

Fig. 11 shows the degree of polarization of the emitted radiation ($\lambda = 4 \ \mu$m) as a function of emission angle for all four wind speeds. The plots have been split so that the left y axis applies to angles less than 60 deg, and the right y axis applies to angles greater than 60 deg. As before, Fig. 11a was computed using $MAXREF = 1$ and therefore does not include reflections whereas Fig. 11b used $MAXREF = 10$ and does include reflections. Overall, the two plots are quite similar. Closer inspection reveals some subtle differences, however. In both figures, at the higher emission angles ($\theta_{\mathrm{e}} > 60°$), the model results show the well known effect that surface roughness and scattering tend to depolarize emitted light. In general, polarization is created by a preferred alignment of the optical elements which interact with the electromagnetic field. A wind-roughened sea surface, however, is made up of more or less randomly oriented individual facets. The Monte Carlo algorithm used here averages together multiple facets (as would any sensor with a finite field of view) which tends to depolarize the integrated signal. At angles below about $50°$ however, the behavior is a little different—increasing roughness slightly increases the polarization. For the direct component of the emission, this effect is due to changes in the observed slope distribution with variations in viewing geometry and wind speed. That is, for angles less than $50°$, roughening the surface tends to increase the effective emission angle $\bar{\chi}$ (see Fig. 7). Since polarization increases with emission angle, the emission from the rougher surface will be more polarized. When surface reflections are included, the polarization is enhanced even more, counter to traditional wisdom which says that multiple scattering tends to depolarize the signal by randomizing any preferred orientation. This result suggests that for a contiguous surface (as opposed to a particulate one; *e.g.*, Henderson et al. (1992)), the facet orientation required to direct reflected rays toward the sensor is such that it enhances the incoming polarization rather than diminish it.

This process can be understood in more detail if we examine the Stokes vectors for each individual ray in a simulation. Recall that the Stokes vector elements

are functions of the amplitudes of the electric vector and the relative phase between them (see Eq. (10)). An alternative definition of the Stokes vector (Kliger et al., 1990) is given by

$$
\begin{aligned}
I &= \langle I \rangle \\
Q &= \langle I_0 - I_{90} \rangle \\
U &= \langle I_{45} - I_{-45} \rangle \\
V &= \langle I_{\mathrm{rcp}} - I_{\mathrm{lcp}} \rangle
\end{aligned}
\tag{24}
$$

where $I_0 - I_{90}$ is the difference in intensities between horizontal and vertical linearly polarized components, $I_{45} - I_{-45}$, is the difference in intensities between linearly polarized components oriented at $+45°$ and $-45°$, and $I_{\mathrm{rcp}} - I_{\mathrm{lcp}}$ is the difference in intensities between right and left circularly polarized components. The angular brackets imply taking a time average, which in this case means averaging together multiple rays. It turns out that the degree of elliptical polarization of thermal emission from a water surface is very small. Thus, we can ignore V when examining the polarization state. Furthermore, recall that we have split up the Stokes vector into polarized and unpolarized parts (Eq. (12)) so that for the polarized portion, $I = \sqrt{Q^2 + U^2}$. Thus, we can get a fairly complete picture of the polarization state of the emitted radiation by looking at just Q and U of each ray individually.

Fig. 12 is a scatter plot of Stokes vectors in the Q-U plane, each point representing the polarized portion of individual rays emitted from a wind-roughened surface. For this plot, we assumed a wind speed of 15 m/s and an emission angle of 70°. In the first run, we set $MAXREF = 1$ and obtained 1000 rays, each represented by a dot. Since a new surface was constructed for each ray, the facet orientation varies from one ray to the next, creating the observed spread in the distribution of dots. Viewed as a vector, the distance of each dot from the origin is a rough measure of the degree of polarization, since $P \approx \sqrt{Q^2 + U^2}/\bar{\epsilon}$. Longer vectors (and therefore greater polarization) correspond to facets with larger emission angles, and shorter vectors (smaller polarization) represent facets with smaller emission angles. Because $MAXREF = 1$, the dots represent only the direct component of the emitted field and give the polarization state of thermal emission from surface roughness without the effects of reflections. The ensemble average of the dots, which represents the time-averaged, effective polarization state of the direct emitted field, is shown by the large circle. For comparison, the Stokes vector for a smooth surface viewed at 70° is represented by the large square. Note that the rough surface has a lower degree of polarization. Although it is convenient to think of roughness randomizing and therefore reducing the preferred polarization state, an alternative explanation is that the polarization is reduced because roughness decreases the effective emission angle for $\theta_{\mathrm{e}} \gtrsim 68°$ (see Fig. 7), which is equivalent to saying that a detector preferentially views those facets which

are leaning toward it. Since polarization increases with emission angle, lower emission angles correspond to lower polarization. A reduced effective emission angle therefore tends to lower the effective polarization state of the emitted radiation.

In the next run, we repeated the 1000 ray simulation on the exact same series of surfaces, but set $MAXREF = 10$ to allow for reflected emission. The rays which did not undergo reflections ($\approx$900) were not plotted since they fall on top of the dots from the previous run. The rays which did undergo reflections are shown by the pluses. Note that the polarization of these rays is in general much greater than that of the direct component. When including reflections, the resultant Stokes vector is given by the sum of direct and reflected components, $\mathbf{S} = \mathbf{S}_e + \mathbf{S}_r$. In the Q-U plane, the two components in general lie in the upper two quadrants so that the vector sum increases the resultant polarization. Including the pluses in the ensemble average therefore tends to enhance the polarization of the average field, which is given by the large plus sign.

4   Conclusion

We modeled the emissivity of a wind-roughened sea surface. By using a ray tracing model, we were able to include the effects of both surface reflections and shadowing. The results show that the reflected component is an important part of the emitted field, affecting nearly 10% of the emitted ray paths and boosting the effective emissivity by as much as 0.03 at higher emission angles for wind speeds $\gtrsim$ 5 m/s. Our model results agree nicely with the recently published sea surface emissivity data of Smith et al. (1996). We also compared our Monte Carlo model to the analytic model of Wu and Smith (1997); our model indicates a smaller reflected component at low wind speeds and larger at higher wind speeds. Using Stokes vectors to quantify the radiation along a given ray path, we computed the polarization of the emitted radiation as well. Surface roughness significantly reduces the polarization for angles > 60° but has a lesser effect at the smaller angles. Including the reflected component has a small but noticeable effect which actually enhances the polarization at intermediate angles.

16

our model. Two anonymous reviewers gave valuable comments which improved the manuscript.

References

Barton, I. J., Zavody, A. M., O'Brien, D. M., Cutten, D. R., Saunders, R. W., Llewellyn-Jones, D. T., 1989. Theoretical algorithms for satellite-derived sea-surface temperatures. J. Geophys. Res. 94, 3365–3375.

Collins, D. G., Wells, M. B., Blattner, W. G., Horak, H. G., 1972. Backward monte-carlo calculations of polarization characteristics of radiation emerging from spherical-shell atmospheres. Appl. Opt. 11 (11), 2684–2696.

Cox, C., Munk, W., 1954. Measurement of the roughness of the sea from photographs of the sun's glitter. J. Opt. Soc. Am. 44 (11), 838–850.

Elfouhaily, T., Chapron, B., Katsaros, K., Vandemark, D., 1997. A unified directional spectrum for long and short wind-driven waves. J. Geophys. Res. 102 (C7), 15781–15796.

Friedman, D., 1969. Infrared characteristics of ocean water (1.5–15 μ). Appl. Opt. 8, 2073–2078.

Hale, G. M., Querry, M. R., 1973. Optical constants of water in the 200-nm to 200-μm wavelength region. Appl. Opt. 12, 555–563.

Hall, F. F., 1964. The polarized emissivity of water in the infrared. Appl. Opt. 3, 781–782.

Henderson, B. G., Jakosky, B. M., Randall, C. E., 1992. A Monte Carlo model of polarized thermal emission from particulate planetary surfaces. Icarus 99, 51–62.

Irvine, W. M., Pollack, J. B., 1968. Infrared optical properties of water and ice spheres. Icarus 8, 324–360.

Jackson, J. D., 1975. Classical Electrodynamics. Wiley, New York.

Jähne, B., Riemer, K. S., 1990. Two-dimensional wave number spectra of small-scale water surface waves. J. Geophys. Res. 95 (C7), 11531–11546.

Kliger, D. S., Lewis, J. W., Randall, C. E., 1990. Polarized Light in Optics and Spectroscopy. Academic Press, New York.

Liu, Y., Yan, X.-H., 1995. The wind-induced wave growth rate and the spectrum of the gravity-capillary waves. J. Phys. Oceanogr. 25, 3196–3218.

Masuda, K., Takashima, T., Takayama, Y., 1988. Emissivity of pure and sea waters for the model sea surface in the infrared window regions. Remote Sens. Environ. 24, 313–329.

Mobley, C. D., 1994. Light and Water: Radiative Transfer in Natural Waters. Academic Press.

Mobley, C. D., 2002. How well does Hydrolight simulate wind-blown sea surfaces? http://www.sequoiasci.com/pdfs/htn1_surfacewaves.pdf.

Otterman, J., Susskind, J., Dalu, G., Kratz, D., Goldberg, I. L., 1992. Effects of water emission anisotropy on multi-spectral remote sensing at thermal

wavelengths of ocean temperature and of cirrus clouds. Appl. Opt. 31, 7633–7646.

Pierson, W. J., Moskowitz, L., 1964. A proposed spectral form for fully developed wind seas based on the similarity theory of S. A. Kitaigorodskii. J. Geophys. Res. 69 (24), 5181–5203.

Preisendorfer, R. W., Mobley, C. D., 1985. Unpolarized irradiance reflectances and glitter patterns of random capillary waves on lakes and seas, by Monte Carlo simulation. NOAA Tech. Memo. ERL PMEL-63.

Preisendorfer, R. W., Mobley, C. D., 1986. Albedos and glitter patterns of a wind-roughened sea surface. J. Phys. Ocean. 16, 1293–1316.

Saunders, P. M., 1967. Shadowing on the ocean and the existence of the horizon. J. Geophys. Res. 72, 4643–4649.

Saunders, P. M., 1968. Radiance of sea and sky in the infrared window 800–1200 cm^{-1}. J. Opt. Soc. Am. 58, 645–652.

Schott, J. R., Brower, B. V., Bhaskar, R., Raqueño, R., Salvaggio, C., 1991. Measurement of the optical properties of materials related to ship signatures. Tech. Rep. RIT/DIRS 90/91-51-140, Rochester Inst. Technol.

Shurcliff, W. A., 1962. Polarized Light: Production and Use. Harvard Univ. Press, Cambridge, MA.

Sidran, M., 1981. Broadband reflectance and emissivity of specular and rough water surfaces. Appl. Opt. 20, 3176–3183.

Smith, W. L., Knuteson, R. O., Revercomb, H. E., Feltz, W., Howell, H. B., Menzel, W. P., Nalli, N. R., Brown, O., Brown, J., Minnett, P., McKeown, W., 1996. Observations of the infrared radiative properties of the ocean— implications for the measurement of sea surface temperature via satellite remote sensing. Bull. Amer. Meteor. Soc. 85, 41–51.

Theiler, J., Henderson, B. G., 1997. A geometrical constraint on shadowing in rough surfaces. Proc. SPIE 3122, 271–279.

Tornow, C., Borel, C. C., Powers, B. J., 1994. Robust water temperature retrieval using multi-spectral and multi-angular IR measurements. In: IGARSS '94. pp. 441–443.

Watts, P. D., Allen, M. R., Nightingale, T. J., 1996. Wind speed effects on sea surface emission and reflection for the along track scanning radiometer. J. Atmos. Oceanic Technol. 13, 126–141.

Wu, X., Smith, W. L., 1997. Emissivity of rough sea surface for 8–13 micron: Modeling and verification. Appl. Opt. 36, 2609–2619.

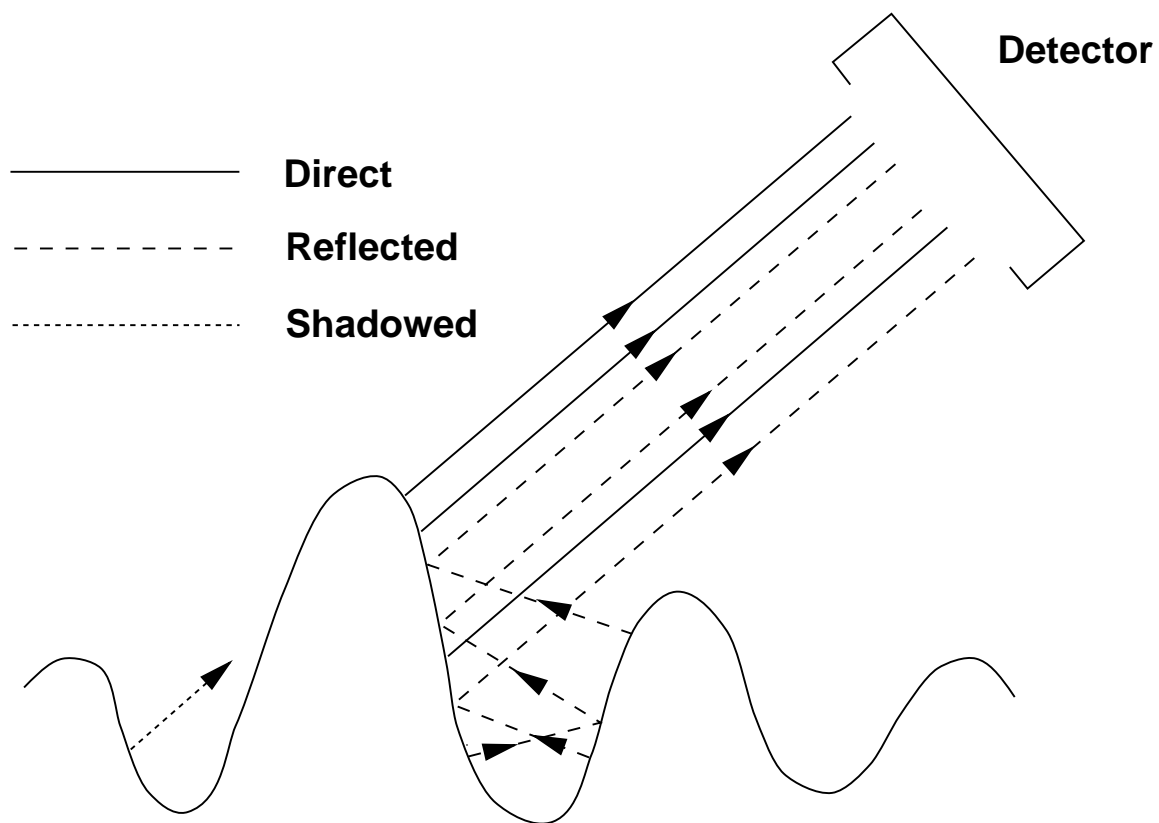Zeisse, C. R., 1995. Radiance of the ocean horizon. J. Opt. Soc. Am. A 12 (9), 2022–2030.

Fig. 1. Schematic diagram of thermal emission from a rough water surface, separating the direct (solid), reflected (dashed), and shadowed (dotted) components of the emitted field. The direct component applies to photons which go straight to the detector and do not interact with other elements of the surface. It represents the emission from surface roughness alone. The reflected component applies to ray paths which have scattered one or more times before reaching the detector. The shadowed rays cannot make it to the detector because they are blocked by intervening wave crests.
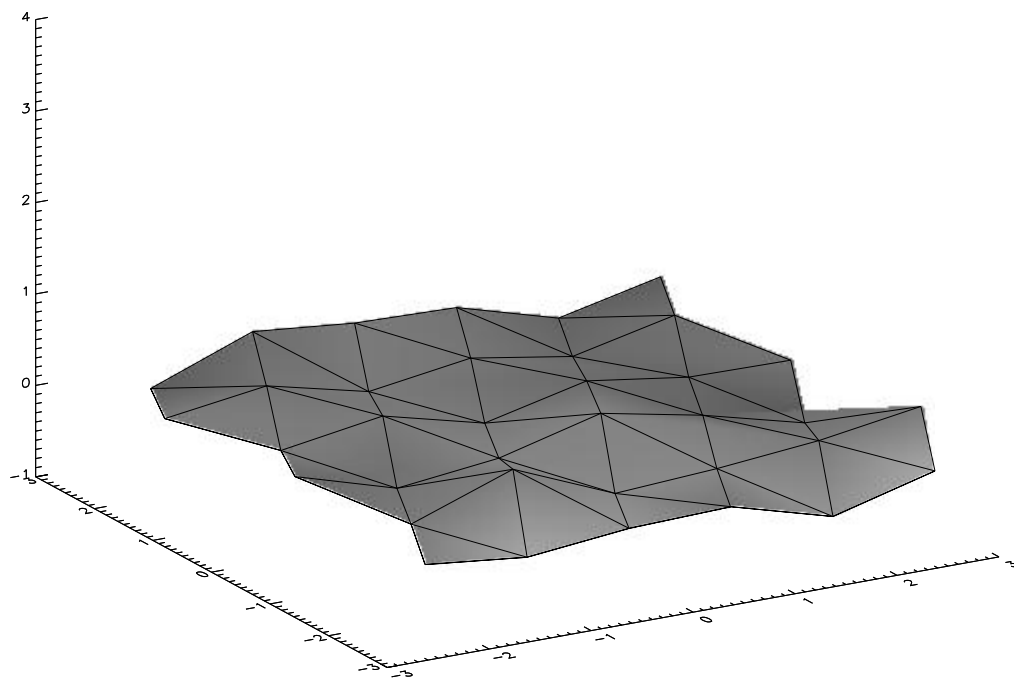
Fig. 2. An example of the rough water surface of Preisendorfer and Mobley (1986) adopted for this study. The actual ray tracing was performed on tessellated surfaces constructed from 20×20 point grids. The surface shown here was constructed from a smaller, 6×6 grid for clarity.
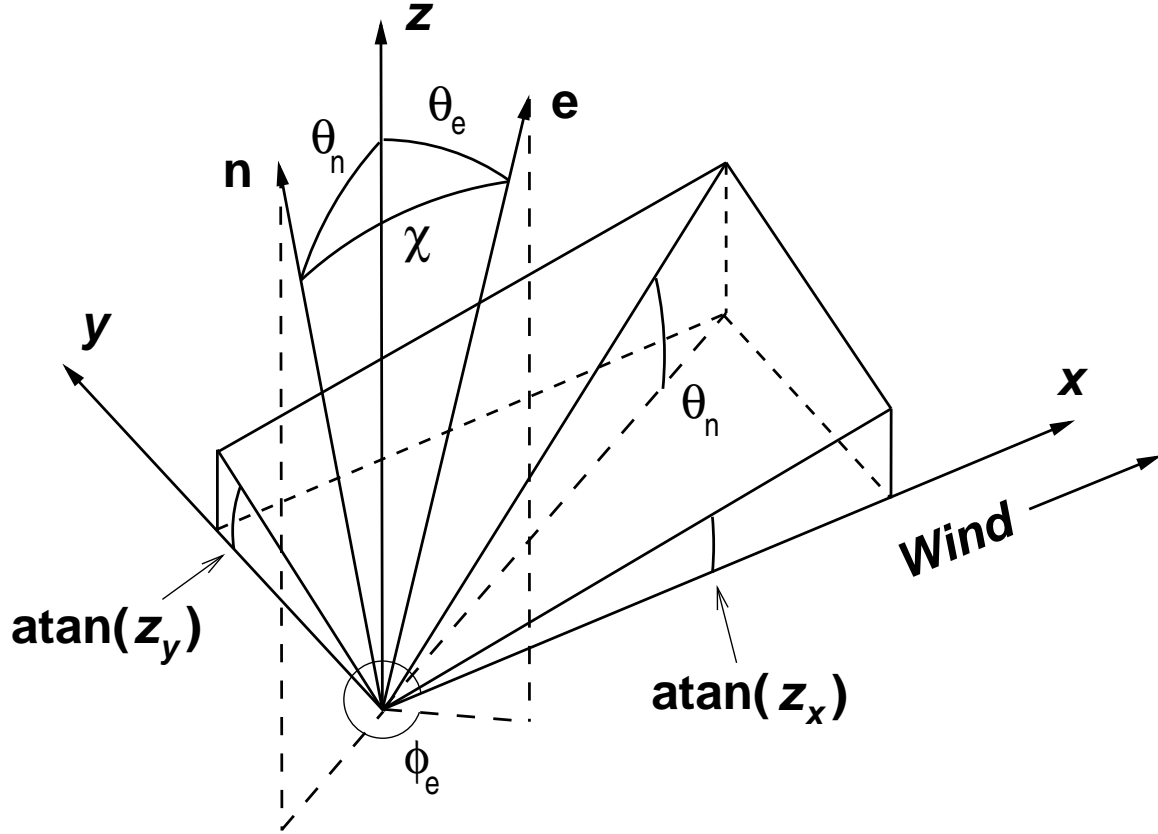
Fig. 3. A sub-section of one triangular facet showing the viewing geometry and associated angles. The facet has normal **n** and is inclined at an angle θ_n relative to the horizontal with slope components $z_x = \partial z/\partial x$ and $z_y = \partial z/\partial y$. The surface is viewed by an observer along the vector **e** with polar angle θ_e and azimuthal angle ϕ_e. θ_e is the emission angle relative to the average surface whereas χ is the emission angle for an individual facet relative to the observer and determines the facet's emissivity for that particular viewing geometry. The wind blows in the positive x direction.
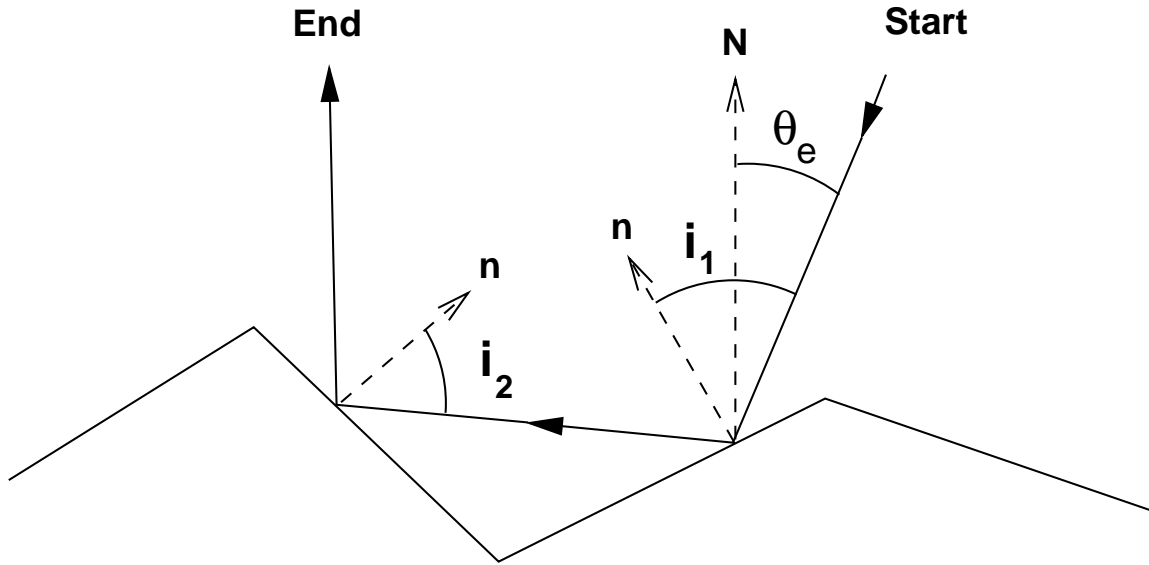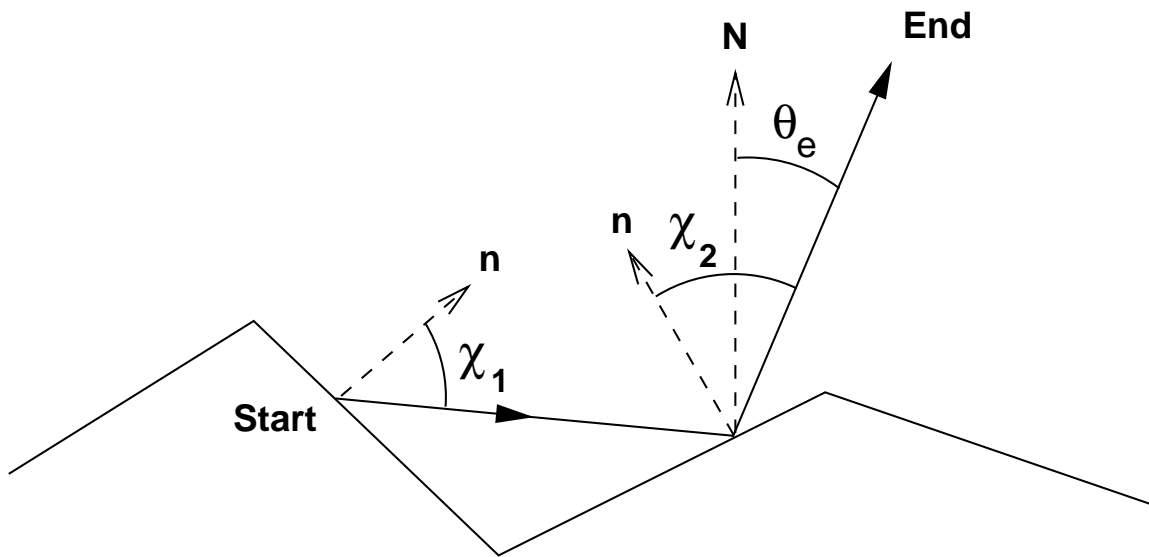
Fig. 4. Figure showing the reverse approach used to calculate the geometry of an individual ray path for emitted photons exiting the surface at an angle θ_e relative to the average surface. In a, the motion is downward from the 'Start' along a ray path defined by the angles θ_e and ϕ_e. Specular reflection is assumed when the ray strikes another facet on the surface. Motion ceases when the ray leaves the surface or reaches a predetermined maximum number of reflections. The emission is computed by reversing the direction of the ray path, using the point of the last reflection ('Start' in b) as the initial source of radiation along the ray.
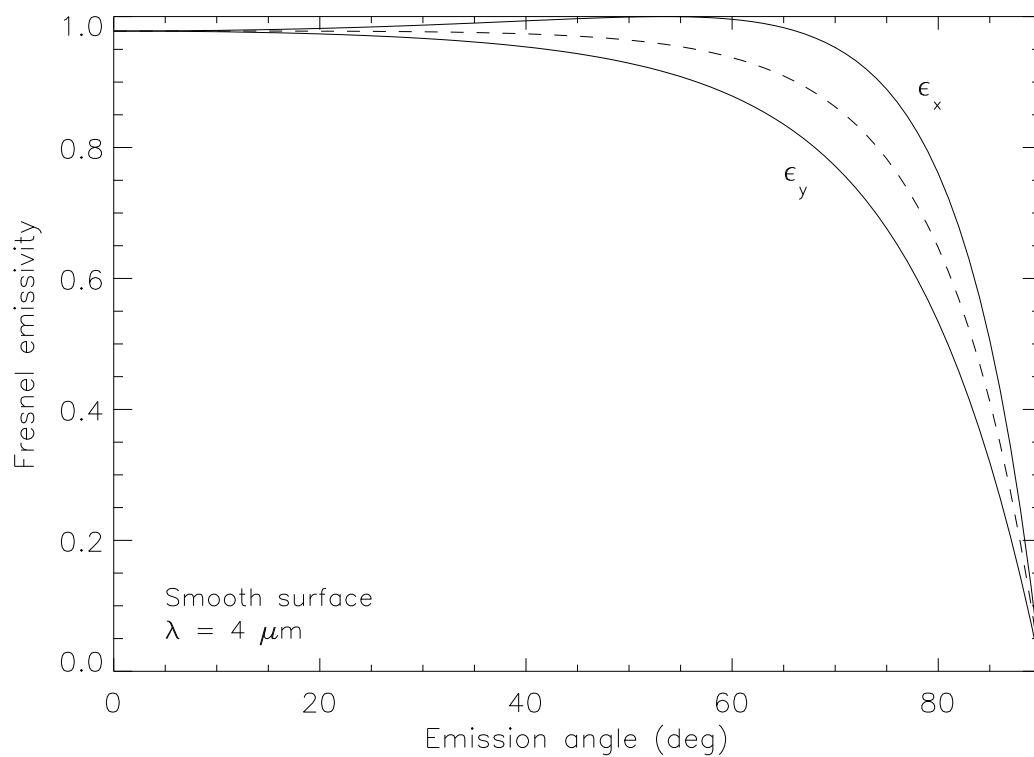
Fig. 5. The Fresnel emissivity of water at $\lambda = 4$ μm showing both the parallel (ϵ_x) and perpendicular (ϵ_y) components. The average of the two is shown by the dashed line.
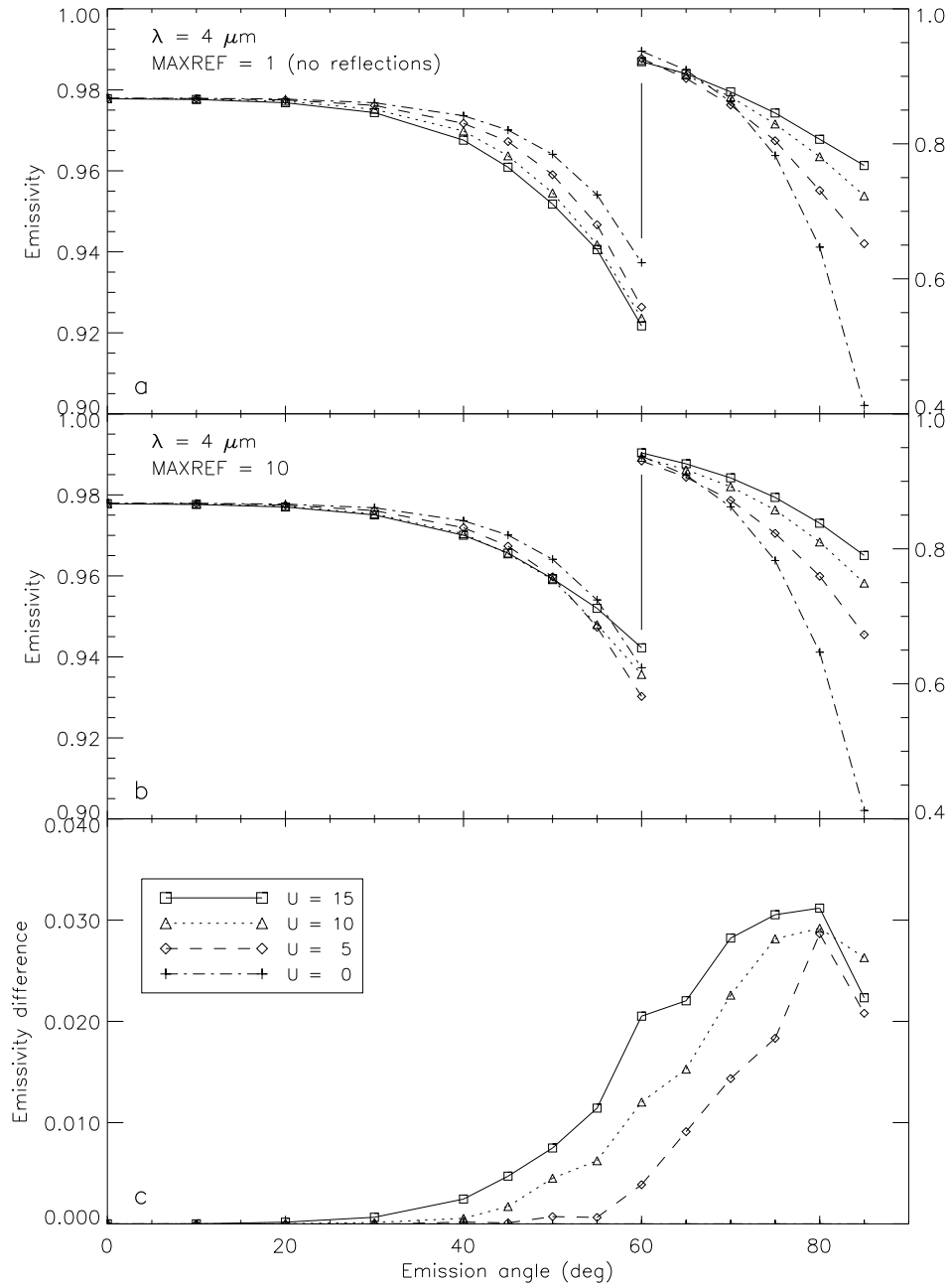
Fig. 6. Directional emissivity of water, $\phi_e = 0°$, at a wavelength of 4 μm for wind speeds of 0, 5, 10, and 15 m/s. The results in a were calculated using a *MAXREF* value of 1 and do not include the reflected component, only direct emission from surface roughness. In b, *MAXREF* was set at 10 and therefore roughness, shadowing, and reflections are all included. In a and b, the left y axis applies to angles 0°–60°, whereas the right y axis applies to angles $\geq 60°$. The difference (b–a) is plotted in c.
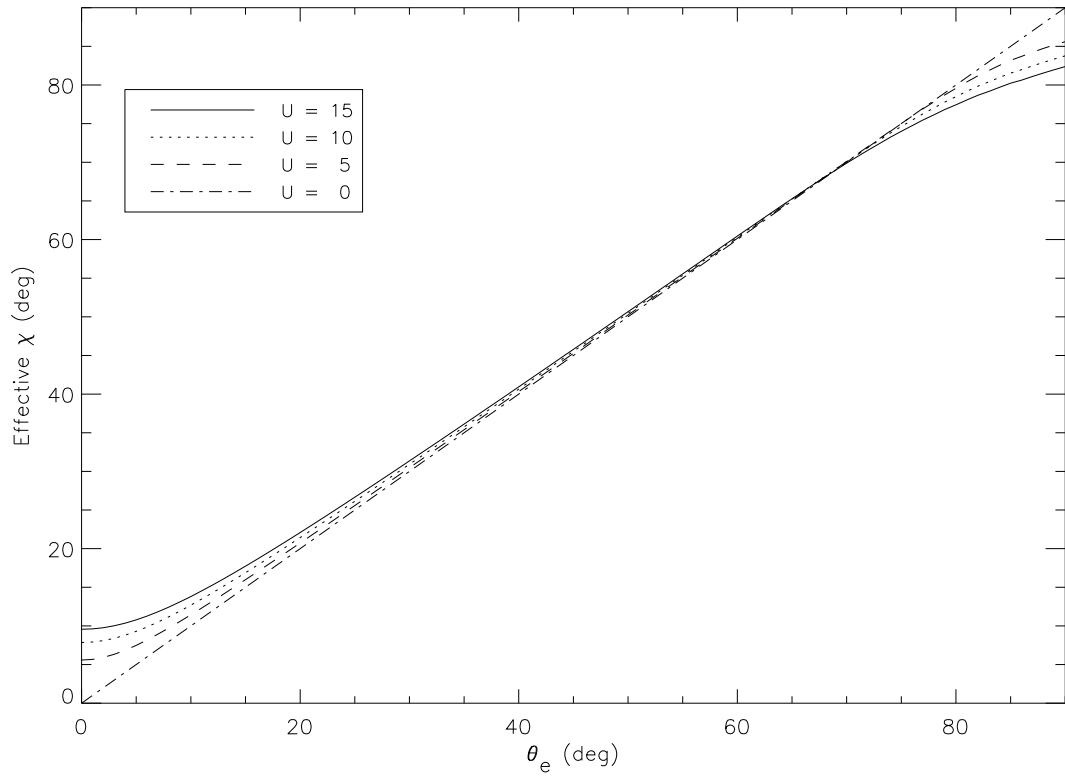
Fig. 7. The effective emission angle, $\bar{\chi}$, plotted as a function of the actual emission angle θ_e at wind speeds of 0, 5, 10, and 15 m/s. The calculation assumed $\phi_e = 0°$.
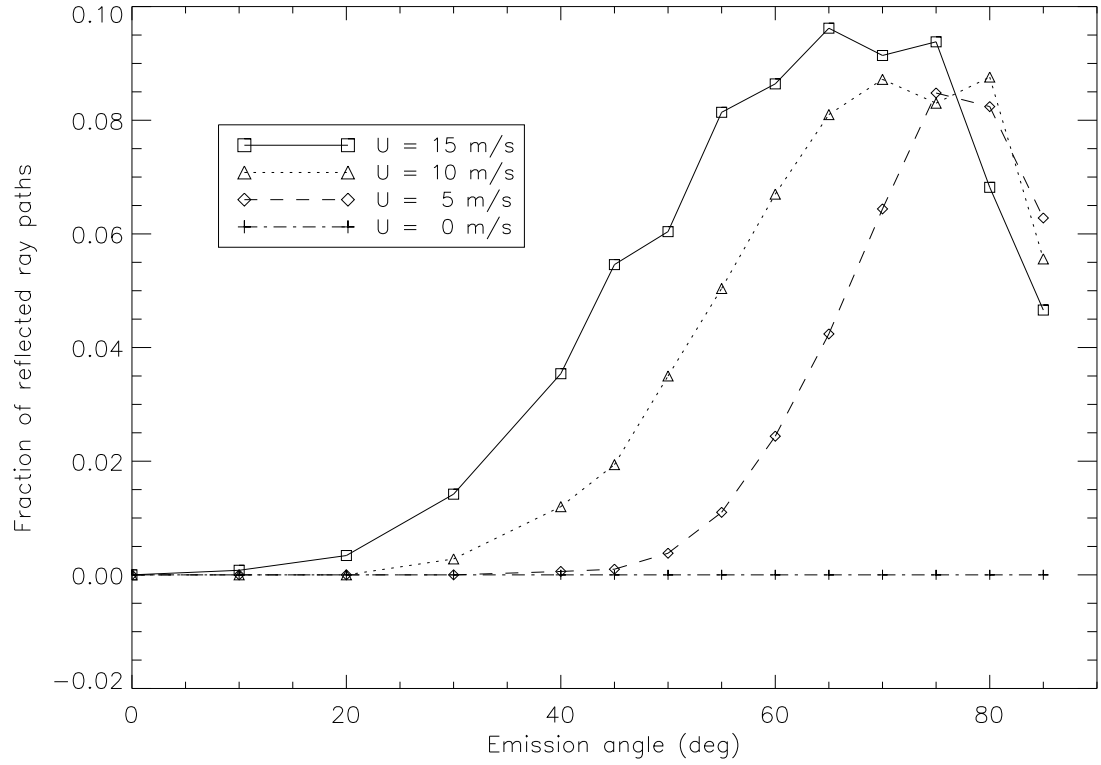
Fig. 8. The fraction of reflected ray paths as a function of emission angle (θ_e) at all four wind speeds ($\phi_e = 0°$). These curves quantify the fraction of the emitted ray paths which reflected off of one or more surface facets after being emitted by the source facet.
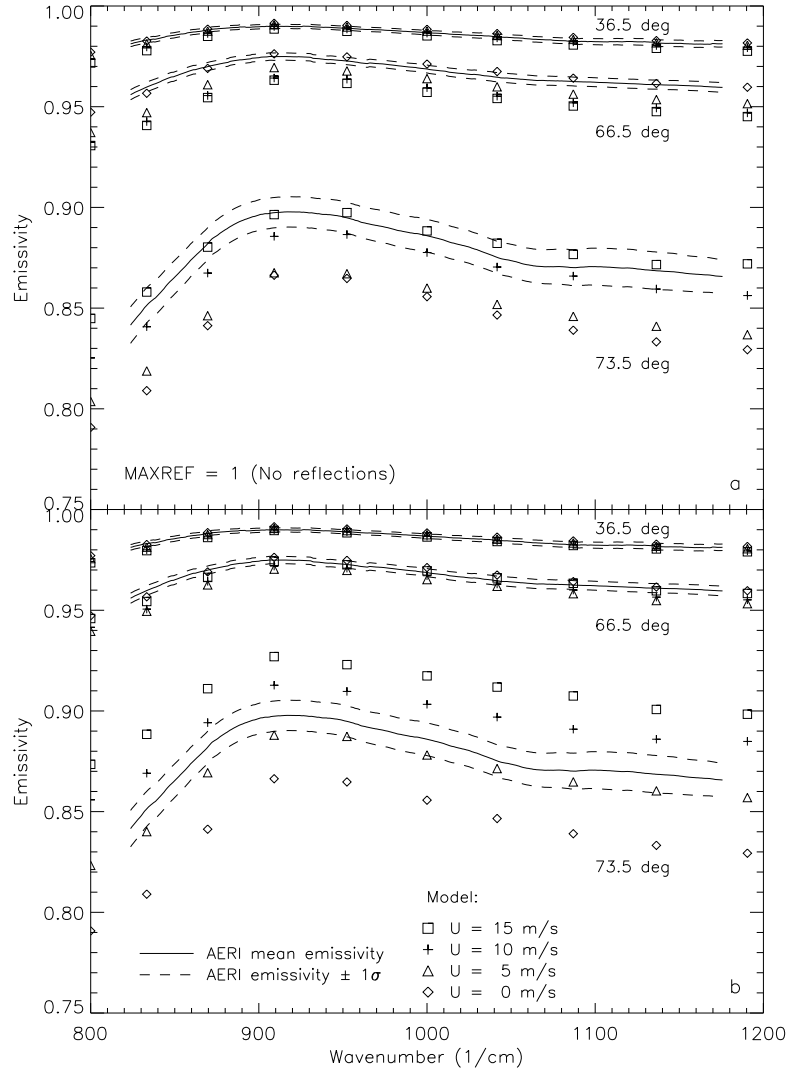
Fig. 9. Spectral emissivity of water computed at emission angles of 36.5°, 66.5°, and 73.5°. The lines are data from Smith et al. (1996) measured from a ship using an Atmospheric Emitted Radiance Interferometer (AERI). The solid lines are the mean of multiple spectra recorded during the day, and the dashed lines are the standard deviation ($\pm 1\sigma$). The symbols are the results from our Monte Carlo model computed at the same emission angles, $\phi_e = 0°$, at wind speeds of 0, 5, 10, and 15 m/s. The model values in a assumed $MAXREF = 1$ and do not include the reflected component, whereas the model values in b assumed $MAXREF = 10$ and do include reflections. Including the reflected component brings the modeled values into agreement with the AERI data and suggest a wind speed of approximately 7 m/s. The actual wind speed varied between 3 and 9 m/s on the day that the data were taken.
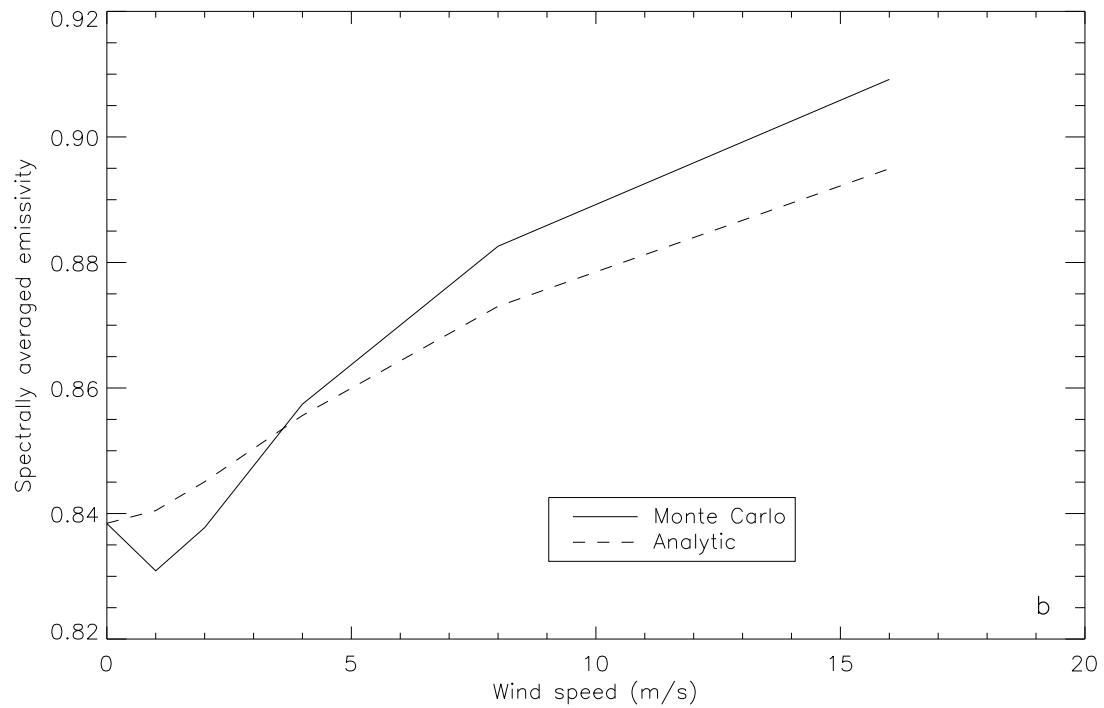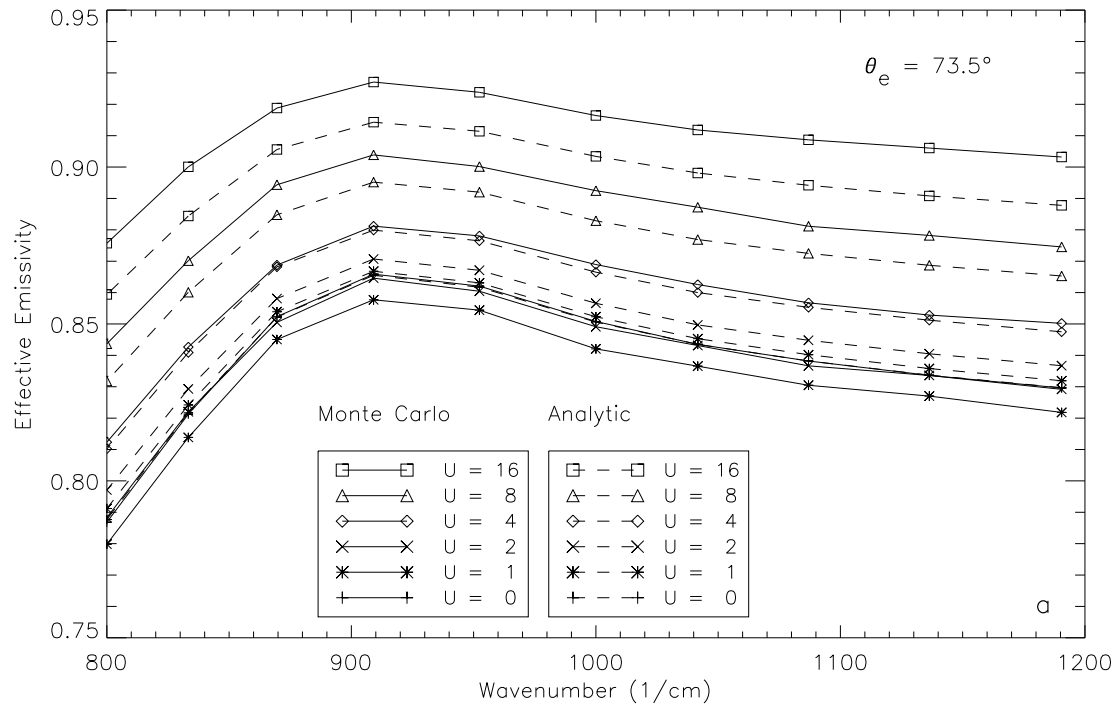
Fig. 10. (a) Comparison of the Monte Carlo results to the analytic model of Wu and Smith (1997) for $\theta_e = 73.5°$. (b) The spectrally averaged emissivity of both models plotted as a function of wind speed.
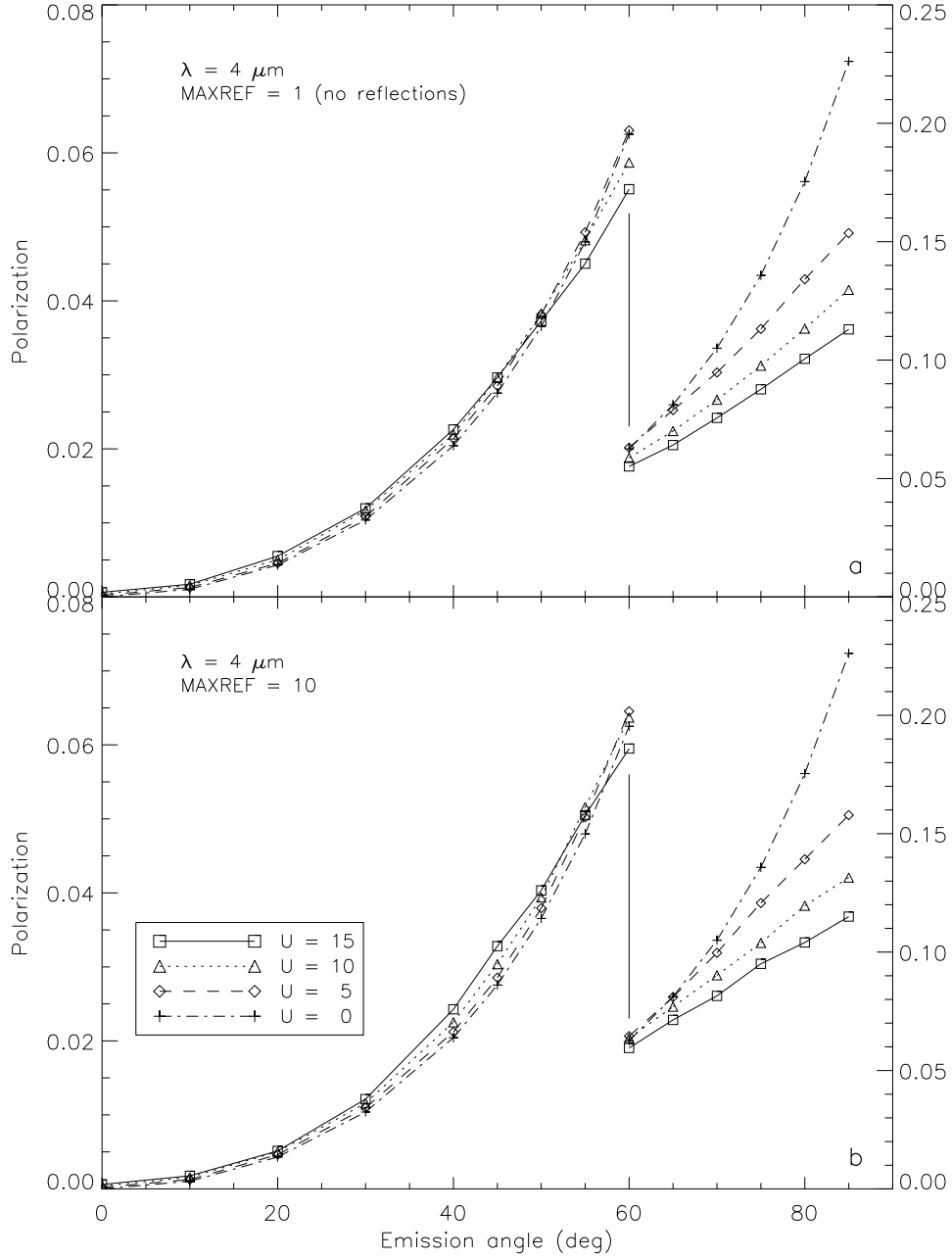
Fig. 11. Directional polarization ($\phi_e = 0°$) computed at a wavelength of 4 μm for wind speeds of 0, 5, 10, and 15 m/s. The values in a were calculated with $MAXREF = 1$ and do not include the effects of the reflected component, whereas in b, $MAXREF = 10$ and the reflected component is included. The left y axis applies to angles 0°–60° whereas the right y axis applies to angles > 60°
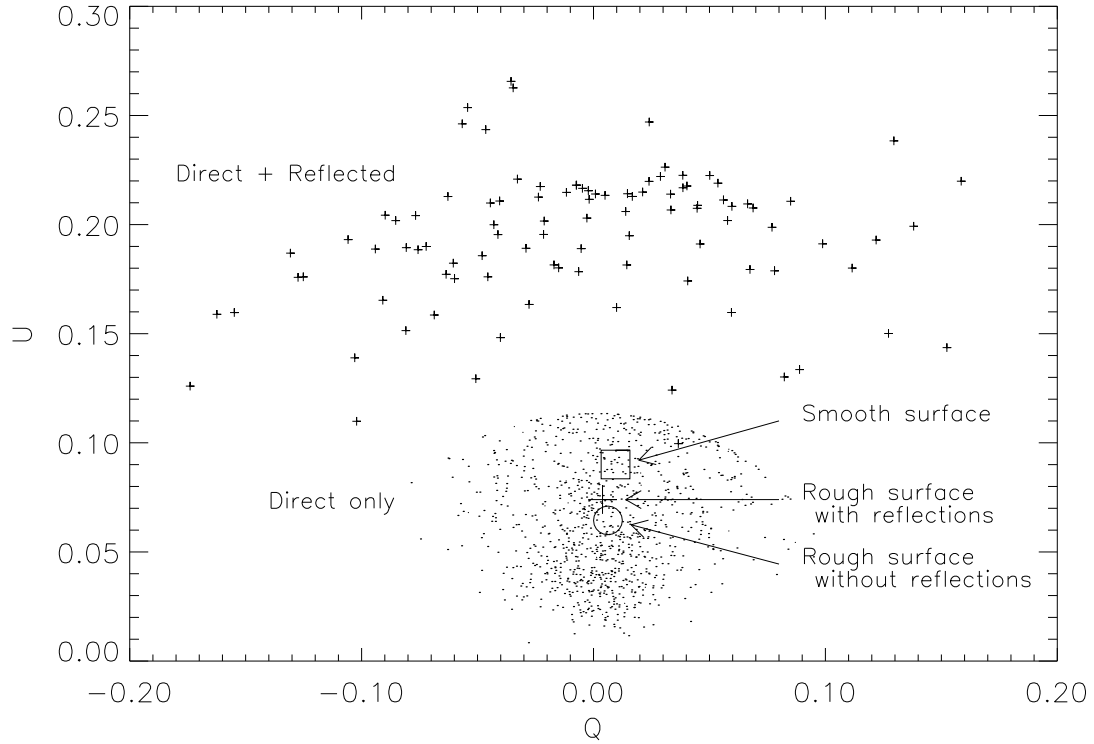
.

Fig. 12. Scatter plot of the Stokes vector elements Q and U for 1000 rays emitted from a surface at a wind speed of 15 m/s, $\theta_e = 70°$ and $\phi_e = 0°$. The 1000 dots were computed with $MAXREF = 1$, the average of which is shown by the large circle. The computations were repeated on the exact same 1000 surfaces with $MAXREF = 10$, and the rays which underwent reflections are shown by the small pluses. The net polarization of this run (which includes all the small pluses and 900 of the dots) is shown by the large plus. The large square shows the Stokes vector elements for a smooth surface.